



**HAL**  
open science

## Searching for multiple populations in Ruprecht 106

H Frelijj, S Villanova, C Muñoz, J. Fernández-Trincado

► **To cite this version:**

H Frelijj, S Villanova, C Muñoz, J. Fernández-Trincado. Searching for multiple populations in Ruprecht 106. Monthly Notices of the Royal Astronomical Society, 2021, 503 (1), pp.867-874. 10.1093/mnras/stab443 . hal-03592209

**HAL Id: hal-03592209**

**<https://hal.science/hal-03592209>**

Submitted on 20 Apr 2023

**HAL** is a multi-disciplinary open access archive for the deposit and dissemination of scientific research documents, whether they are published or not. The documents may come from teaching and research institutions in France or abroad, or from public or private research centers.

L'archive ouverte pluridisciplinaire **HAL**, est destinée au dépôt et à la diffusion de documents scientifiques de niveau recherche, publiés ou non, émanant des établissements d'enseignement et de recherche français ou étrangers, des laboratoires publics ou privés.

# Searching for multiple populations in Ruprecht 106

H. Freljić<sup>1</sup>,<sup>1</sup>★ S. Villanova,<sup>1</sup> C. Muñoz<sup>1,2,3</sup>★ and J. G. Fernández-Trincado<sup>4,5,6</sup>

<sup>1</sup>*Departamento de Astronomía, Casilla 160-C, Universidad de Concepción, Chile*

<sup>2</sup>*Departamento de Astronomía, Universidad de La Serena, Av. Juan Cisternas 1200, La Serena, Chile*

<sup>3</sup>*Instituto de Investigación Multidisciplinario en Ciencia y Tecnología, Universidad de La Serena. Avenida Raúl Bitrán S/N, La Serena, Chile*

<sup>4</sup>*Instituto de Astronomía y Ciencias Planetarias, Universidad de Atacama, Copayapu 485, Copiapó, Chile*

<sup>5</sup>*Institut Utinam, CNRS UMR 6213, Université Bourgogne-Franche-Comté, OSU THETA Franche-Comté, Observatoire de Besançon, BP 1615, F-25010 Besançon Cedex, France*

<sup>6</sup>*Centro de Investigación en Astronomía, Universidad Bernardo O'Higgins, Avenida Viel 1497, Santiago, Chile*

Accepted 2021 February 10. Received 2021 February 8; in original form 2021 January 1

## ABSTRACT

More than a decade has passed since the definition of globular cluster (GC) changed, and now we know that they host multiple populations (MPs). But few GCs do not share that behaviour and Ruprecht 106 is one of these clusters. We analysed 13 member red giant branch stars using spectra in the wavelength range 6120–6405 Å obtained through the GIRAFFE Spectrograph, mounted at UT2 telescope at Paranal, as well as the whole cluster using *C*, *V*, *R*, and *I* photometry obtained through the Swope telescope at Las Campanas. Atmospheric parameters were determined from the photometry to determine Fe and Na abundances. A photometric analysis searching for MPs was also carried out. Both analyses confirm that Ruprecht 106 is indeed one of the few GCs to host simple stellar population, in agreement with previous studies. Finally, a dynamical study concerning its orbits was carried out to analyse the possible extragalactic origin of the cluster. The orbital integration indicates that this GC belongs to the inner halo, while an energy plane shows that it cannot be accurately associated with any known extragalactic progenitor.

**Key words:** stars: abundances – Hertzsprung–Russell and colour–magnitude diagrams – stars: imaging – globular clusters: individual: Ruprecht 106 – Galaxy: kinematics and dynamics.

## 1 INTRODUCTION

The classical paradigm of Galactic globular clusters (GCs) being simple stellar populations (SSPs) has changed dramatically by observational evidence. The presence of chemical inhomogeneities in its light elements, like a spread in Na or O extensively studied by Carretta et al. (2009), led some authors to create different theories to try to explain this behaviour (D’Ercole et al. 2008; Bastian et al. 2013; Renzini et al. 2015), but, to date, no one satisfies all the observations. As mentioned, the abundance analysis (obtained through spectroscopy) like the Na–O, Mg–Al, and C–N anticorrelation is one of the strongest weapons to determine whether a GC possesses multiple population (MPs) since different populations present different chemical abundances.

Photometry is a different approach to search for MPs when chemical abundances are not available. We can use it to analyse large groups of stars simultaneously since UV filters have proved to be sensitive to differences in chemical abundances of light elements. Bedin et al. (2004) used *HST* observations to prove that using the right combination of filters, it is possible to distinguish between multiple main sequences and/or subgiant and/or giant branches in almost all GCs. The most popular works involving this technique was Piotto et al. (2015), who used an improved combination of the UV/blue WFC3/UVIS filters *F275W*, *F336W*, and *F438W*, the

so-called ‘magic trio’, to analyse 60 GCs. All of them presented splitted CMD sequences or, at least, a great broadening in some parts of the sequences. Other filters like the *C* filter from the Washington Filter system (Canerna 1976) have proved to be very sensitive in discriminating the presence of MPs (Cummings et al. 2014; Freljić et al. 2017). But like most cases, there seem to be an exception to the rule. A bunch of GCs seems to host an SSP [i.e. E3 (Salinas & Strader 2015), Terzan 7 (Tautvaišienė et al. 2004), Ruprecht 106 (Villanova et al. 2013), etc.], although actually some of them do not have enough evidence to confirm this hypothesis. In this paper, we are going to focus in one of these: Ruprecht 106 (hereafter Rup106).

According to Harris (1996, 2010 edition), Rup106 is a GC with  $\alpha(J2000)$ : 12<sup>h</sup>38<sup>m</sup>40<sup>s</sup>.2 and  $\delta(J2000)$ : -51°09′01″, located at 21.2 kpc from the Sun and 18.5 kpc from the Galactic Centre. It has a metallicity  $[Fe/H] = -1.68$ , an heliocentric radial velocity,  $RV = -44 \pm 3$  km s<sup>-1</sup>, and a foreground reddening  $E(B - V) = 0.2$ .

As mentioned, Villanova et al. (2013, hereafter V13) realized a spectroscopic study in Rup106 showing that all the nine samples studied did not show an Na–O anticorrelation, concluding that Rup106 is one of the few GCs that fail to exhibit the phenomenon of MPs, which have been well supported by an independent photometric study by Dotter et al. (2018). V13 also show that Rup106 has an extragalactic origin since its very low Na and  $\alpha$ -element abundances only match those of the Magellanic Clouds and of the Sagittarius Galaxy. Both studies together present strong evidence of Rup106 host an SSP, but the nine targets from V13 are not enough to assure that the cluster has no chemical spread at all. This paper tries to provide, along with V13, enough spectroscopic and photometric

\* E-mail: heinzfreljic@udec.cl (HF); Cesar.alejandro.munoz.g@gmail.com (CM)

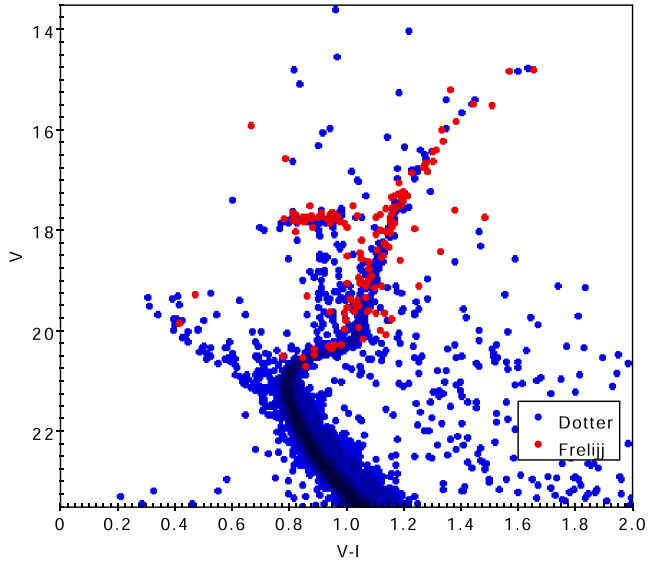


**Figure 1.** Plot overlapping a CMD using  $V_{\text{ground}} - I_{\text{ground}}$  versus  $V_{\text{ground}}$  from Dotter et al. (2011) and CMD with our calibrated  $V - I$  versus  $V$ .

evidence to demonstrate that Rup106 is indeed an SSP cluster or that possess at least one star from a different population, what could open again the controversy about this cluster.

This paper is organized in this way: In Section 2, we discuss our observations and data reduction from photometry and spectroscopy. In Section 3, we detail the steps done to get heliocentric velocities and proper motions (PMs) to filter our photometric catalogue from non-members. We also describe the process we used to get the atmospheric parameters that are necessary to calculate abundances. Section 4 describes the abundance determination. Section 5 presents the photometric analysis we applied to determine either Rup106 have MPs or not. Section 6 contains a study of the orbits discussing the possible extragalactic origin of Rup106. Section 7 presents a resume of our results.

## 2 DATA

### 2.1 Photometric observations

The sample used for this work is composed of 21 photometric images taken at the 1-m Swope telescope, Las Campanas Observatory, Chile. All of these images are from the same observing run in 2014 March. The Swope telescope works with one CCD (E2V CCD231-84) that contains four amplifiers together forming a square of  $4096 \times 4112$  pixels with a scale of  $0.435 \text{ arcsec pixel}^{-1}$  and a field of view of  $29.7 \times 29.8 \text{ arcmin}^2$ . The filters used for this work are the Washington  $C$  filter (Cantenna 1976), the  $I_{\text{KC}}$  filter, and the Harris  $V$  and  $R$  filters. From the 21 images, 2 images were taken using the  $I$  filter, 5 using  $R$ , 6 images using  $V$ , and 8 using  $C$ .

Details of the exposure time for different filters used are as follows:

|     | $N^\circ$ (exposure time) (s) |
|-----|-------------------------------|
| $C$ | 1(30), 1(300), 6(1200)        |
| $V$ | 2(10), 1(100), 3(400)         |
| $R$ | 1(10), 1(100), 3(400)         |
| $I$ | 1(10), 1(100)                 |

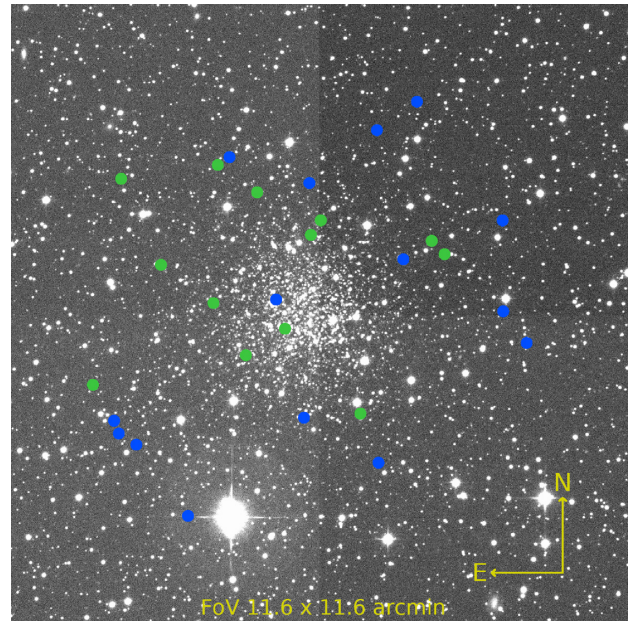
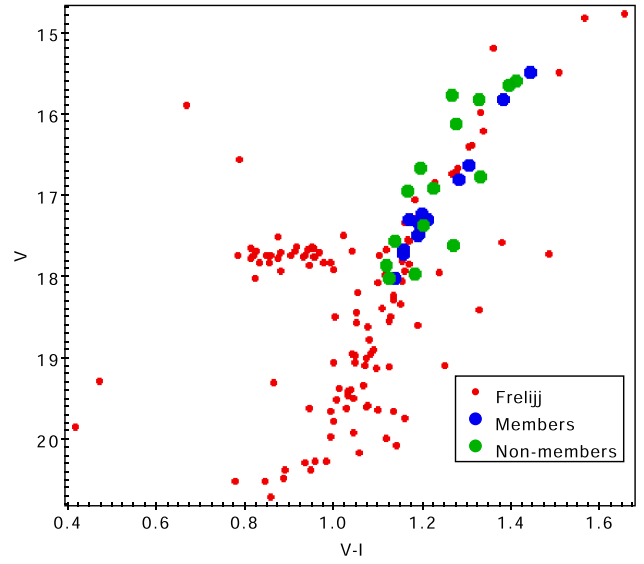


**Figure 2.** Top panel: cluster targets have been highlighted in the CMD. Members are shown as green dots while non-members are shown as blue dots. Bottom panel: spatial distribution of the same targets along the cluster.

The full width at half-maximum (FWHM) of the images ranges between 1.37 and 2.15 arcsec and the airmasses vary between 1.079 and 1.160. None of the nights were considered hotometric, hence standard fields could not be observed.

The data processing and reduction was performed according to Frelíj et al. (2017). We used IRAF<sup>1</sup> to process all the four quadrants of each image separately, more specifically its tasks ccdproc, zerocombine, and flatcombine. After that a script was used

<sup>1</sup>IRAF is distributed by the National Optical Astronomy Observatory, which is operated by the Association of Universities for Research in Astronomy (AURA) under a cooperative agreement with the National Science Foundation.

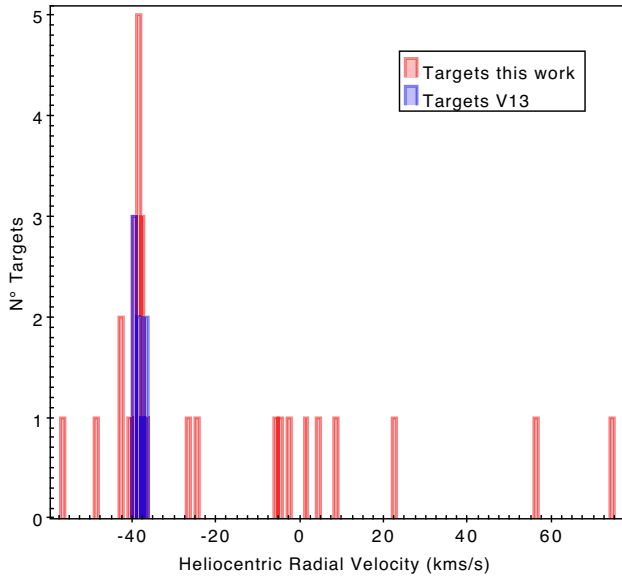


**Figure 3.** Heliocentric velocities of the targets of this study are represented in red, and targets from V13 have been overlapped in blue. All targets between  $-45$  and  $-35$   $\text{km s}^{-1}$  are considered members of the cluster.

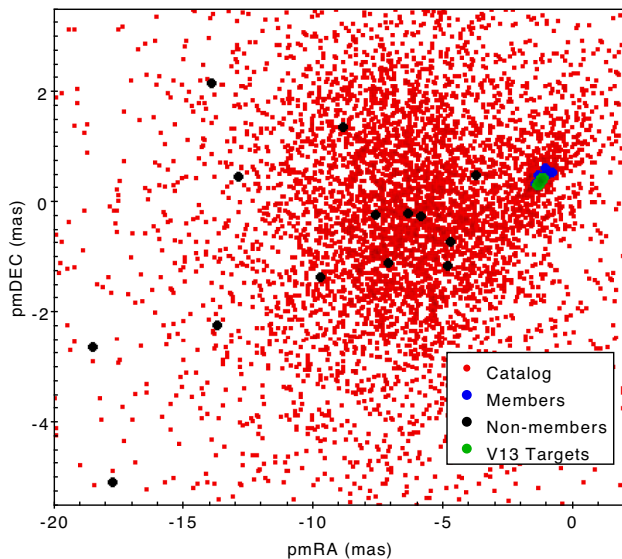


**Figure 4.** PMs for each star of the catalogue. Blue dots represent the 13 targets members of the cluster, black dots represent discarded non-members targets, and green dots represent the targets from V13.

to combine the four quadrants into one single image. The photometry was performed using DAOPHOT (Stetson 1987) since this program is the indicated to threat crowded fields. We obtained the PSF using the brightest non saturated and isolated stars in each frame. With a good PSF at hand, we proceeded to run ALLSTAR in each image separately. Once finished, we aligned all the catalogues with DAOMATCH and DAOMASTER. The file with the transformation coordinates was used along with the images, the catalogues, and psf files to finally run ALLFRAME (Stetson 1994). ALLFRAME made PSF-photometry simultaneously in all the frames to realize the best photometry. Finally, with each image catalogue that ALLFRAME returned, we apply aperture corrections realizing aperture photometry to the PSF-stars and comparing it with the PSF-photometry.

We calibrated our data using the catalogue used in Dotter, Sarajedini & Anderson (2011) available in the ACS GC Treasury data base, where they took the filters  $F606W$  and  $F814W$  and converted them into ground-based filters  $V$  and  $I$  (hereafter  $V_{\text{ground}}$  and  $I_{\text{ground}}$ ) using the relation from Sirianni et al. (2005). After matching them with our catalogue, we derived the transformation equations in the form of

$$V = (v - i) \times m + b + v,$$

$$I = (v - i) \times m + b + i,$$

Where  $V$  and  $I$  are our calibrated magnitudes,  $m$  is the slope,  $b$  is the  $y$ -intercept of the line, and  $v$  and  $i$  our instrumental magnitudes. To verify the accuracy of the calibration, we calculated the difference  $V_{\text{ground}} - V$  and  $I_{\text{ground}} - I$ . For the  $I$  filter, we found a residual shift of 0.04 mag, so we subtracted it to all the calibrated  $I$  magnitudes. Fig. 1 shows a comparison between the  $V_{\text{ground}} - I_{\text{ground}}$  versus  $V_{\text{ground}}$  CMD from the Dotter et al. (2011) catalogue (blue dots) and our calibrated catalogue (red dots), both HB and RGB are aligned, probing that the calibration is fine. We could not find a way to calibrate  $C$  and  $R$  filters, but for this, it was not necessary.

Bonatto, Campos & Kepler (2013) show that this cluster has a mean differential reddening of  $\langle E(B - V) \rangle = 0.026 \pm 0.010$  with a maximum differential reddening of  $\delta E(B - V)_{\text{max}} = 0.051$ , indicating that we do not need to make differential reddening corrections.

Finally, the  $x/y$  coordinates of the standardized catalogue were transformed to RA/Dec.(J2000) using the xy2sky task from WCSTOOLS and a World Coordinate System created using 10 well-separated stars from the reference frame with the IRAF tasks ccmmap and ccsetwcs.

## 2.2 Spectroscopic observations

Our spectroscopic data consist of observations from 2017 as part of the programme ID 098.D-0227(A) obtained using the medium-high-resolution FLAMES-GIRAFFE Spectrograph installed in the UT2 (Kueyen) telescope in Paranal. The resolving power is  $R \sim 26\,400$ . Our targets were selected in the magnitude range  $V = 15.5$  and  $18.5$  and they belong to the RGB (Fig. 2). We observed 28 stars in the Wavelength range  $6120\text{--}6405$   $\text{\AA}$ . The exposure time was 2640 s per spectrum, and each star was observed four times, getting a total of 112 spectra.

The spectroscopic data were reduced using the GIRAFFE pipeline, with only a normalization, sky subtraction, and a transformation from nm to  $\text{\AA}$  remaining to do. These steps were done using IRAF tasks, specifically continuum, sarith, and hedit. The four spectra of each star were combined using the task scombine to improve the S/N ratio.

We measured observed RVs using the IRAF fxcor package, with the help of a synthetic spectrum as a template calculated using typical RGB star parameters, i.e.  $T_{\text{eff}} = 4500$  K,  $\log(g) = 1.50$ ,  $v_t = 1.50$   $\text{km s}^{-1}$ , and the metallicity of the cluster ( $[\text{Fe}/\text{H}] = -1.50$ ). These relative velocities were used to apply Doppler corrections through the IRAF task dopcor.

## 3 DATA ANALYSIS

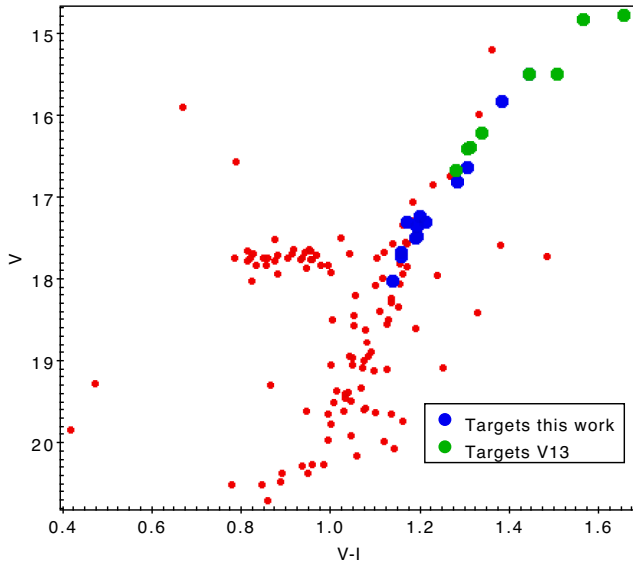
### 3.1 Heliocentric RVs, PMs, and membership

We obtained heliocentric RVs using the IRAF task rvcorrect. According to Fig. 3, we consider possible cluster members those targets with RV between  $-45$  and  $-35$   $\text{km s}^{-1}$ . This reduced our targets to 15. The mean heliocentric velocity of this sample is  $-38.99 \pm 1.6$   $\text{km s}^{-1}$  with a standard deviation of  $1.7$   $\text{km s}^{-1}$ .

**Table 1.** The details of the targets.

| ID      | RA(J2000)<br>(h:m:s) | Dec.<br>(°:′:″) | <i>V</i><br>(mag) | <i>I</i><br>(mag) | pmRA<br>(mas yr <sup>-1</sup> ) | pmDEC<br>(mas yr <sup>-1</sup> ) | RV<br>(km s <sup>-1</sup> ) | $T_{\text{eff}}$<br>(K) | log( <i>g</i> )<br>(dex) | $v_t$<br>(km s <sup>-1</sup> ) |
|---------|----------------------|-----------------|-------------------|-------------------|---------------------------------|----------------------------------|-----------------------------|-------------------------|--------------------------|--------------------------------|
| 11012   | 12:38:33.50          | -51:10:58.30    | 18.022            | 16.885            | -1.470 79                       | 0.343 99                         | -39.16                      | 4978                    | 2.3715                   | 1.4564                         |
| 11579   | 12:39:05.60          | -51:10:26.60    | 17.303            | 16.093            | -1.243 88                       | 0.381 64                         | -37.88                      | 4856                    | 2.0253                   | 1.5678                         |
| 12911   | 12:38:42.58          | -51:09:23.00    | 15.494            | 14.054            | -1.373 53                       | 0.356 48                         | -39.25                      | 4382                    | 1.0307                   | 1.8881                         |
| 14650   | 12:38:57.47          | -51:08:11.40    | 17.231            | 16.033            | -1.076 49                       | 0.607 63                         | -40.31                      | 4843                    | 1.9899                   | 1.5792                         |
| 14861   | 12:38:23.50          | -51:07:58.40    | 17.484            | 16.292            | -1.4267                         | 0.316 29                         | -38.29                      | 4888                    | 2.1132                   | 1.5396                         |
| 15108   | 12:38:25.04          | -51:07:43.40    | 17.502            | 16.315            | -1.267 08                       | 0.400 51                         | -42.77                      | 4891                    | 2.1220                   | 1.5367                         |
| 15225   | 12:38:39.52          | -51:07:37.10    | 17.673            | 16.517            | -1.3498                         | 0.488 73                         | -39.50                      | 4920                    | 2.2042                   | 1.5103                         |
| 15502   | 12:38:38.34          | -51:07:20.70    | 16.807            | 15.526            | -1.187 59                       | 0.385 36                         | -37.29                      | 4761                    | 1.7783                   | 1.6474                         |
| 15985   | 12:38:45.98          | -51:06:49.40    | 16.631            | 15.328            | -1.129 86                       | 0.474 52                         | -38.71                      | 4723                    | 1.6877                   | 1.6766                         |
| 16174   | 12:39:02.27          | -51:06:34.50    | 17.725            | 16.570            | -0.943 86                       | 0.507 56                         | -38.09                      | 4928                    | 2.2292                   | 1.5022                         |
| 16394   | 12:38:50.70          | -51:06:18.80    | 15.822            | 14.439            | -1.098 52                       | 0.466 12                         | -38.02                      | 4501                    | 1.2368                   | 1.8218                         |
| 5015399 | 12:38:47.27          | -51:09:52.90    | 17.351            | 16.159            | -0.828 73                       | 0.548 44                         | -37.87                      | 4865                    | 2.0487                   | 1.5603                         |
| 5016747 | 12:38:51.17          | -51:08:54.20    | 17.305            | 16.137            | -1.275 74                       | 0.341 61                         | -42.74                      | 4856                    | 2.0264                   | 1.5675                         |

*Note.* The order of the columns are star ID, Right Ascension (J2000), Dec. (J2000), magnitude in *V*, magnitude in *I*, absolute PM in RA, absolute PM in Dec., heliocentric RV, effective temperature, surface gravity, and microturbulence velocity.

**Figure 5.** Definitive CMD, targets from this work appear as blue dots while targets from V13 are the green dots.

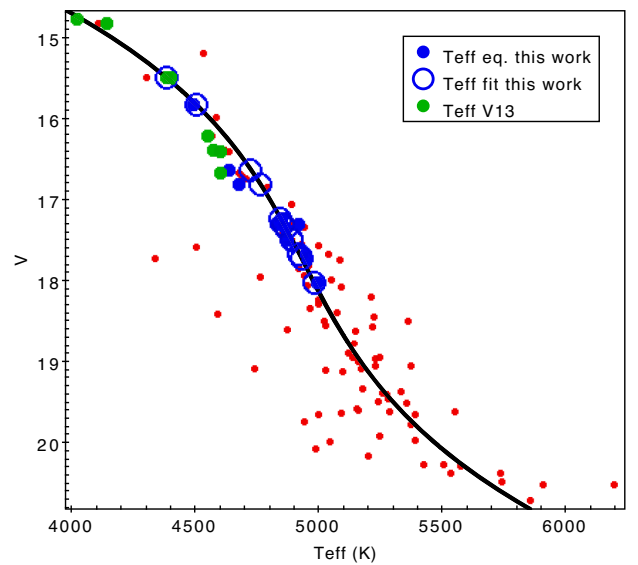
These values are in good agreement with V13, as it is shown in Fig. 3.

Thanks to the PMs provided by the *Gaia* mission (Gaia Collaboration et al. 2016, 2018), we could remove further non-member stars as shown in Fig. 4. We discarded two more of our targets that had RV similar to the mean RV of the cluster but very different PM. The average PM of our targets are pmRA =  $-1.21 \pm 0.13$  and pmDEC =  $0.43 \pm 0.08$  mas yr<sup>-1</sup>.<sup>2</sup> Table 1 lists the details of the final members.

### 3.2 Atmospheric parameters

Fig. 5 shows the *V* – *I* versus *V* CMD with the identified members from this work and V13. All the stars with photometric errors greater than 0.1 were removed.

<sup>2</sup>In agreement with *Gaia* EDR3 (Gaia Collaboration et al. 2020).

**Figure 6.** Effective temperatures for each RGB star are shown. Average value from Alonso et al. (1999) and Ramírez & Meléndez (2005) appear as red dots. A polynomial fit is shown in black, filled blue dots indicate targets from this work obtained through the mentioned relations, blue circles are the values obtained through the polynomial fit, and green dots are the effective temperatures from V13.

A reddening correction  $E(B - V) = 0.20$  (2010 edition Harris 1996) was applied to the *V* – *I* colour using the extinction relation  $E(B - V) = 1.24E(V - I)$  in order to obtain effective temperatures. Then  $T_{\text{eff}}$  were determined averaging the values obtained from the expressions given in Ramírez & Meléndez (2005) and Alonso, Arribas & Martínez-Roger (1999). Since Alonso et al. (1999) work with Johnson colours, a relation

$$(V - I)_J = -0.005 + 1.273 \times (V - I)_C$$

from Fernie (1983) was applied to our *V* – *I* colour. Then  $T_{\text{eff}}$  were plotted against *V* and a polynomial was adjusted to the RGB, making possible to obtain  $T_{\text{eff}}$  using the *V* magnitudes instead of *V* – *I*, reducing the uncertainties. These values obtained through the polynomial fit are our definitive  $T_{\text{eff}}$ . Fig. 6 shows a comparison

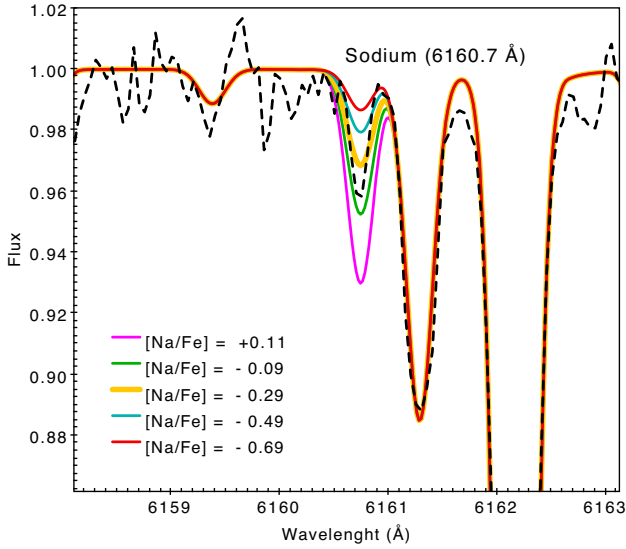


**Figure 7.** Spectrum-synthesis in the line at 6160.7 Å of the star 12911. Five different synthetic spectra appear as coloured lines. The best fit among these is shown as a broader yellow line ([Na/Fe] = -0.29).

**Table 2.** Table with abundance values.

| ID      | $T_{\text{eff}}$ | [Fe/H] | [Na/Fe] |
|---------|------------------|--------|---------|
| 11012   | 4978             | -1.42  | < -0.20 |
| 11579   | 4856             | -1.44  | -0.39   |
| 12911   | 4382             | -1.53  | -0.29   |
| 14650   | 4843             | -1.43  | < -0.29 |
| 14861   | 4888             | -1.41  | < -0.01 |
| 15108   | 4891             | -1.47  | < 0.05  |
| 15225   | 4920             | -1.55  | < 0.03  |
| 15502   | 4761             | -1.47  | -0.31   |
| 15985   | 4723             | -1.46  | < -0.16 |
| 16174   | 4928             | -1.42  | -0.37   |
| 16394   | 4501             | -1.53  | -0.28   |
| 5015399 | 4865             | -1.44  | -0.44   |
| 5016747 | 4856             | -1.46  | -0.41   |

*Notes.* The order of the columns are star ID, effective temperature, metallicity, and Na abundance. In some cases, we could establish only upper limits for Na abundances..

between the  $T_{\text{eff}}$  obtained through the formulas and the polynomial,  $T_{\text{eff}}$ , from V13 are shown for comparison.

Surface gravities  $\log(g)$  were determined through the canonical equation:

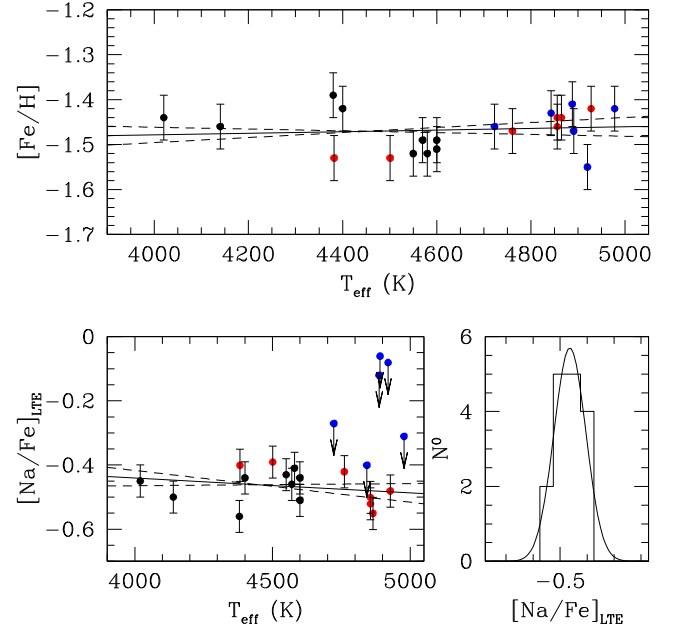
$$\log(g/g_{\odot}) = 4\log(T_{\text{eff}}/T_{\odot}) - \log(L/L_{\odot}) + \log(M/M_{\odot}).$$

Assuming a mass of 0.8  $M_{\odot}$ , a luminosity based in the distance modulus  $(m - M)_v = 17.25$  (2010 edition Harris 1996) and a relation obtained from Alonso et al. (1999) for bolometric corrections (BC). Finally, microturbulence velocities  $v_t$  were determined using the relation from Gratton, Carretta & Castelli (1996):

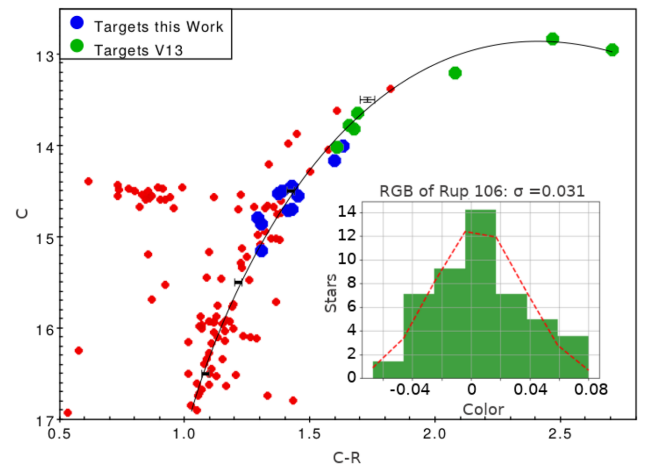
$$v_t = 2.22 - 0.322 \times \log(g).$$

Table 1 gives the values of the atmospheric parameters.

The  $T_{\text{eff}}$ ,  $\log(g)$ , and  $v_t$  were used together with the metallicity [Fe/H] = -1.5 (V13) to generate atmospheric models for each target.



**Figure 8.** Upper panel: [Fe/H] abundance as a function of the temperature. Lower panel (left-hand side): [Na/Fe]<sub>LTE</sub> abundances as a function of the temperature. Lower panel (right-hand side): [Na/Fe]<sub>LTE</sub> distribution.



**Figure 9.** CMD using the Washington filter  $C$  to distinguish the presence of MPs; the spread of the targets along the RGB indicates the presence of only one population. A fiducial has been adjusted, colour differences of stars from the fiducial have been normalized in a histogram, and the best-fitting Gaussian has been derived.

#### 4 ABUNDANCE ANALYSIS

Chemical abundances were calculated using the local thermodynamic equilibrium (LTE) program MOOG (Snedden 1973), and atmospheric models were calculated using the ATLAS9 code (Kurucz 1970), assuming our initial estimations of the atmospheric parameters. The spectrum-synthesis technique was used to determine Fe and Na abundances. This method consists of comparing an observed spectral line with five different synthetic spectra calculated with different abundances. The interpolated model with the lowest root mean square give us the abundance of the element associated with that line. For a more precise determination, we applied a parabolic fit to the five rms values of the five synthetic spectra plotted as a function

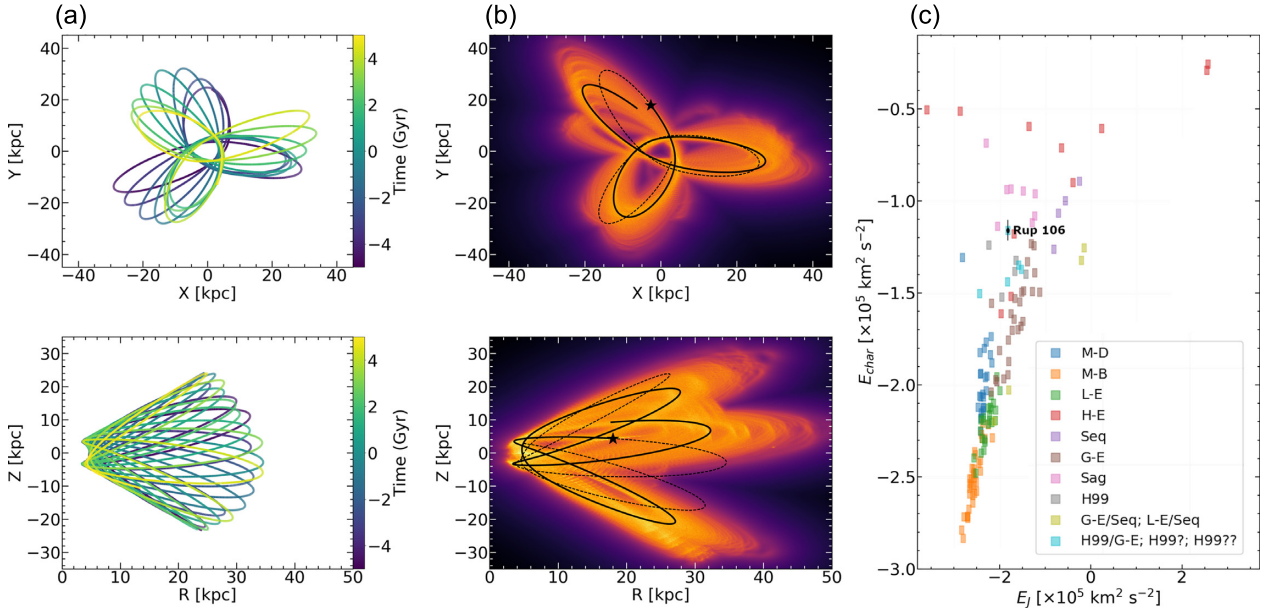


**Figure 10.** Panels (a) and (b) show the equatorial and meridional Galactic planes in the inertial frame, time-integrated forward/backward over 5 Gyr. Panel (b) shows the probability density, with yellow and orange colours corresponding to more probable regions of the space, which are crossed more frequently by the simulated orbits. The black solid and dashed lines show the forward and backward orbital path of Rup106 over 1 Gyr, for guidance. Panel (c) shows the characteristic orbital energy ( $(E_{\max} + E_{\min})/2$ ) versus the orbital Jacobi constant ( $E_J$ ) in the non-inertial reference frame where the bar is at rest. Other Galactic GCs associated with different progenitors from (Massari, Koppelman & Helmi 2019) are shown for comparison. The black dot with error bars refers to Rup106 analysed in this work.

of the abundance in order to obtain the minimum. This minimum is the final abundance we assumed for the line.

We used the following lines for iron: (6136, 6191, 6213, 6252, 6322, 6335, 6336, and 6393 Å), while for Na, we used the line at 6160.7 Å since that at 6154.2 Å was too weak. The FWHM to be used for the spectrum-synthesis of the Na line was determined by the comparison of the synthetic spectra with nearby strong and well-defined Ca and Fe lines. An example of the spectrum-synthesis applied to the Na line is shown in Fig. 7. For some targets, we could estimate only upper limits. The adopted solar abundances were  $\log\epsilon(\text{Fe}) = 7.50$  and  $\log\epsilon(\text{Na}) = 6.32$  (V13). Our mean abundances for each star are represented in Table 2. Na is known to be affected by departure from LTE. In this paper, we did not apply any NLTE correction since our analysis is based on the relative Na abundance of stars that have roughly the same atmospheric parameters and so the same NLTE corrections for sodium. In any case, according to the INSPECT data base,<sup>3</sup> the Na NLTE correction for our abundances is of the order of  $-0.20$  dex for all our targets.

Fig. 8 reports the present results together with those of V13. In the upper panel, we report the  $[\text{Fe}/\text{H}]$  abundance as a function of the temperature. We can see that there is no trend in spite that the two sets of abundances were obtained using different spectrographs and methods. Also, the linear fit is compatible with a flat trend with  $1\sigma$ . Combining the two data bases, we obtained a mean iron abundance of

$$[\text{Fe}/\text{H}] = -1.47 \pm 0.01$$

and

$$\sigma_{[\text{Fe}/\text{H}]} = 0.05 \pm 0.01.$$

<sup>3</sup><http://www.inspect-stars.com/>

In the lower panels, we report the  $[\text{Na}/\text{Fe}]_{\text{LTE}}$  abundances as a function of the temperature (left-hand panel) and the  $[\text{Na}/\text{Fe}]_{\text{LTE}}$  distribution (right-hand panel). In this case, GIRAFFE data have a systematic shift of  $+0.11$  dex (targets with upper limits were not considered for the comparison). The cause of this systematics is probably due to the fact that in V13 we used the four Na lines at 5682.6, 5688.2, 6154.2, and 6160.7 Å as Na abundance indicator, while here we could use only that at 6160.7 Å, systematics due to some effect related to the spectrograph not well removed during the reduction procedure cannot be ruled out such as scattered light. We applied a correction of  $-0.11$  dex to the Na abundances obtained from GIRAFFE data. We found a mean Na LTE abundance of

$$[\text{Na}/\text{Fe}] = -0.47 \pm 0.01.$$

The Na distribution histogram is very narrow with an rms of

$$\sigma_{[\text{Na}/\text{Fe}]} = 0.06 \pm 0.01.$$

The typical internal error on the fit for our  $T_{\text{eff}}$  is 10–20 K, while the errors on  $\log(g)$  and  $v_t$  are below 0.1 dex and  $0.05 \text{ km s}^{-1}$ , respectively. If we apply the same procedure described in V13 for the error calculation, we obtain

$$\sigma_{\text{TOT}}(\text{Na}) = 0.05.$$

We underline the fact that in our case, the observational error is dominated by the S/N of the spectra. Comparing this value with the rms of the Na distribution histogram, we can confirm the result by V13 that Rup106 does not host multiple stellar populations.

## 5 PHOTOMETRIC ANALYSIS

As mentioned, the Washington filter *C* has proved to be useful to detect MPs due to the fact that it covers CN and NH bands (Cantnera 1976). Fig. 9 shows a CMD obtained using the Washington Filter *C*

combined with the  $R_{KC}$  filter, limited to the part of the RGB where our targets lie. If Rup106 had more than one stellar population, we should observe one of the following effects:

- (i) A split in the RGB (Cummings et al. 2014). In this case, all the targets would lie in one of the RGBs.
- (ii) A spread in the RGB caused by the chemical differences between the populations and larger than the photometric errors.

Fig. 9 shows instead that the RGB of Rup106 is very narrow and that the spread in colour is compatible with the errors.

A fiducial curve (defined as the highest density locus of stars along the RGB) has been fitted along the RGB in  $C - R$  versus  $C$  (the black curve in 9). We then measured the colour difference of the stars from the fiducial and build a distribution histogram of this value. We then derived the best-fitting Gaussian for the histogram and got  $\sigma = 0.031 \pm 0.003$ , about 1.5 times the median error in the  $C - R$  colour for the RGB that is  $\sigma_{C-R} = 0.02 \pm 0.01$ ,

obtained calculating the square root of the sum of the squares of the errors of each filter. The  $\sigma$  value we found is very likely an upper limit and not the intrinsic width of the RGB since the field contamination cannot be fully removed because of the superposition of the cluster with the field in the PM space (see Fig. 4). For this reason, we conclude that the width of the Rup106 RGB is fully explained by the photometric errors and does not require the presence of multiple stellar populations.

## 6 THE ORBIT

We used the GRAVPO16<sup>4</sup> model (Fernández-Trincado et al., in preparation) to study the orbital elements (eccentricity, apo-/perigalactocentric distance, the characteristic orbital energy, and the orbital Jacobi constant) of Rup106. Since V13 already show that this cluster has an extragalactic origin based on its Na and  $\alpha$ -element abundances, the aim is to find the Halo structure Rup106 is associated with.

The GRAVPO16 is composed of a massive ( $\sim 1.1 \times 10^{10} M_{\odot}$ ) 'boxy/peanut' bar/bulge structure accompanied by multiple stellar discs whose profiles mimic to that of the Besançon Galaxy model (Robin et al. 2003, 2014). For the orbit computations, we adopt the same model configuration and Sun's positions and velocity as in Fernández-Trincado et al. (2020), except for the bar patterns speed, which we adopt the recommended value of  $41 \text{ km s}^{-1} \text{ kpc}^{-1}$  (see e.g. Sanders, Smith & Evans 2019). We integrated hundred thousand orbits by adopting a simple Monte Carlo approach that considers the errors in the observables as  $1\sigma$  variations over a 5-Gyr time-span toward the past (backward) and future (forward) by adopting the observables with their respective errors from Baumgardt et al. (2019):

- (i) RA: 189:6675;
- (ii) Dec.:  $-51^{\circ}150'27''$ ;
- (iii)  $d = 21.2 \pm 2.12 \text{ kpc}$ ;
- (iv)  $RV_{\text{Helio}} = -38.36 \pm 0.26 \text{ km s}^{-1}$ ;
- (v)  $pm_{\text{RA}} = -1.25 \pm 0.01 \text{ mas yr}^{-1}$ ;
- (vi)  $pm_{\text{DEC}} = 0.39 \pm 0.01 \text{ mas yr}^{-1}$ .

Fig. 10 shows the resulting orbits of Rup106 on the equatorial and meridional Galactic planes in the inertial frame. The top and bottom panels in Fig. 10(a) show the predicted orbit of Rup106 without considering the errors in the observable, while the top and bottom

panels in Fig. 10(b) show the resulting ensemble of orbits from our Monte Carlo approach, which consider the errors in the observable. The yellow and orange colours correspond to more probable regions of the space, which are crossed more frequently by the simulated orbits, while the black solid and dashed lines show the forward and backward orbital path of Rup106 over 1 Gyr for guidance.

Figs 10(a) and (b) reveal that Rup106 lies on a radial and highly eccentric ( $> 0.81 \pm 0.01$ ) halo-like orbit with rather higher excursions above the Galactic plane ( $\sim 23.6 \pm 3.2 \text{ kpc}$ ). The perigalactocentric ( $r_{\text{min}}$ ) and apogalactocentric ( $r_{\text{max}}$ ) distance of Rup106 is  $\sim 3.4 \pm 0.5$  and  $\sim 32.7 \pm 3.7 \text{ kpc}$ , respectively, placing the cluster well within the inner halo of the Milky Way, but located beyond of the bulge/bar region. In addition, using a slightly different angular velocity for the bar ( $\pm 10 \text{ km s}^{-1} \text{ kpc}^{-1}$ ) does not change significantly our conclusions, and returns orbits in which the cluster is confined to the inner halo.

It is important to note that unlike Baumgardt et al. (2019), our orbit computations are based in a realistic (as far as possible) barred Milky Way model, which may affect the orbital path of Rup106, as the cluster orbit has close approaches ( $\sim 3 \text{ kpc}$ ) to the 'bulge/bar' region, where the strength of the 'bar' structure is important.

Fig. 10(c) shows the Characteristic orbital energy ( $E_{\text{char}} = (E_{\text{max}} + E_{\text{min}})/2$ ) versus the orbital Jacobi constant ( $E_J$ ) in the non-inertial reference frame where the bar is at rest, as defined in Moreno, Pichardo & Schuster (2015) and Fernández-Trincado et al. (2020). This plane reveals that the orbit of Rup106 lies in the boundary between three groups of GCs, e.g. those in the high-energy group (H-E), the group dominated by Helmi-Stream (H99), and the group associated with the Sagittarius dwarf galaxy (Sgr; see e.g. Massari et al. 2019). For this reason, based only in the dynamical configuration of Rup106, there is no clear association with any of the proposed progenitors in the Milky Way.

V13 concluded that the very low Na and  $\alpha$ -element abundances of Rup106 only match those of the Magellanic Clouds and of the Sagittarius Galaxy. Combining our results with these conclusions we could determine that the progenitor of Rup106 is the Sagittarius dwarf galaxy, adding evidence that does not contradict the results from Bellazzini, Ferraro & Ibata (2003) and are in line with those from Sbordone et al. (2005), however it still contradicts the conclusion of Law & Majewski (2010) who did not find significant evidence for association with any wrap of the Sgr arms, leaving the discussion opened again.

In spite of the fact that the progenitor of Rup106 is not clear, Massari et al. (2019) and Bajkova & Bobylev (2020) define it as a potential Helmi-Stream (H99) member. It is worth mentioning that all the other members of this group possess MPs with the exception of E3 (although only classified as H99 by Massari et al. 2019). This cluster was studied in Salinas & Strader (2015) and Monaco et al. (2018) analysing 23 RGB members with low-resolution spectroscopy and four RGB with high-resolution spectroscopy, respectively. Both studies conclude that there is no evidence of MPs in such cluster.

In addition, Bastian & Lardo (2018) named other three SSP GCs: Terzan 7, Pal 12, and Pal 3. The first two GCs are Sgr members and the last belongs to the H-E group. This would indicate that all the SSP and potential SSP GCs have an extragalactic origin.

## 7 CONCLUSIONS

In this paper, we have derived atmospheric parameters and chemical abundances for Fe and Na for 13 RGB stars of the GC Rup106 using FLAMES-GIRAFFE data. The abundance results have been compared with V13. A photometric analysis with images taken from

<sup>4</sup><https://gravpot.utinam.cnrs.fr/>

the 1-meter Swope Telescope was done as a complement to the spectroscopic results. For this purpose, we studied the broadening of the RGB of Rup106 in the CMD using a filter sensible to the presence of MPs. Finally, we studied the orbit of the cluster and tried to associate it with some known halo stream.

From these studies, we can conclude the following:

(1) Rup106 has  $[Fe/H] = -1.47 \pm 0.01$  and  $[Na/Fe]_{LTE} = -0.47 \pm 0.01$ . The  $[Fe/H]$  is in good agreement with V13, and the Na abundances confirm that the cluster does not have multiple stellar populations.

(2) The  $RGB_{Broadening}/RGB_{error}$  ratio in the colour–magnitude diagram of Rup106 is 1.5. This indicates that although there is a difference between both values, it is not enough large to contradict the spectroscopic result.

(3) The orbital analysis indicates that Rup106 is confined to the halo, while the orbital energy puts Rup106 among the H-E group, Helmi-Stream (H99), and Sagittarius dwarf galaxy (Sgr).

It is interesting to note that combining our results concerning the orbits with the analysis from V13, we could propose the Sagittarius dwarf galaxy as the progenitor of Rup106. However, the work made in Law & Majewski (2010) indicates the opposite, leaving the question open.

## ACKNOWLEDGEMENTS

We thank the referee for helpful comments that greatly improved this paper. SV gratefully acknowledges the support provided by Fondecyt regular n. 1170518. JGF-T is supported by FONDECYT No. 3180210. HF acknowledges financial support from Agencia Nacional de Investigación y Desarrollo (ANID) grant 21181653. CM thanks the support provided by FONDECYT No. 1181797 and from the Chilean Centro de Excelencia en Astrofísica y Tecnologías Afines (CATA) BASAL grant AFB-170002.

## DATA AVAILABILITY

This work has made use of data from the European Space Agency (ESA) mission *Gaia* (<https://www.cosmos.esa.int/gaia>), processed by the *Gaia* Data Processing and Analysis Consortium (DPAC; <https://www.cosmos.esa.int/web/gaia/dpac/consortium>). Funding for the DPAC has been provided by national institutions, in particular the institutions participating in the *Gaia* Multilateral Agreement.

This work has made use of data from the ACS GC Survey available from the ACS GC Treasury data base.

The spectroscopic raw data analysed here were observed under the Programme 098.D-0227(A) and can be obtained from the ESO Science archive.

The Photometric raw data analysed in this paper will be shared on reasonable request to the corresponding author (HF).

## REFERENCES

Alonso A., Arribas S., Martínez-Roger C., 1999, *A&AS*, 140, 261  
Bajkova A. T., Bobylev V. V., 2020, preprint ([arXiv:2008.13624](https://arxiv.org/abs/2008.13624))

Bastian N., Lardo C., 2018, *ARA&A*, 56, 83  
Bastian N., Lamers H. J. G. L. M., de Mink S. E., Longmore S. N., Goodwin S. P., Gieles M., 2013, *MNRAS*, 436, 2398  
Baumgardt H., Hilker M., Sollima A., Bellini A., 2019, *MNRAS*, 482, 5138  
Bedin L. R., Piotto G., Anderson J., Cassisi S., King I. R., Momany Y., Carraro G., 2004, *ApJ*, 605, L125  
Bellazzini M., Ferraro F. R., Ibata R., 2003, *AJ*, 125, 188  
Bonatto C., Campos F., Kepler S. O., 2013, *MNRAS*, 435, 263  
Cantena R., 1976, *AJ*, 81, 228  
Carretta E. et al., 2009, *A&A*, 505, 117  
Cummings J. D., Geisler D., Villanova S., Carraro G., 2014, *AJ*, 148, 27  
D’Ercole A., Vesperini E., D’Antona F., McMillan S. L. W., Recchi S., 2008, *MNRAS*, 391, 825  
Dotter A., Sarajedini A., Anderson J., 2011, *ApJ*, 738, 74  
Dotter A., Milone A. P., Conroy C., Marino A. F., Sarajedini A., 2018, *ApJ*, 865, L10  
Fernández-Trincado J. G., Chaves-Velasquez L., Pérez-Villegas A., Vieira K., Moreno E., Ortigoza-Urdaneta M., Vega-Neme L., 2020, *MNRAS*, 495, 4113  
Ferne J. D., 1983, *PASP*, 95, 782  
Frelíj H., Geisler D., Cummings J., Cohen R. E., Mauro F., Muñoz C., Villanova S., Tang B., 2017, *MNRAS*, 472, 4532  
Gaia Collaboration et al., 2016, *A&A*, 595, A1  
Gaia Collaboration et al., 2018, *A&A*, 616, A1  
Gaia Collaboration, Brown A. G. A., Vallenari A., Prusti T., de Bruijne J. H. J., Babusiaux C., Biermann M., 2020, preprint ([arXiv:2012.01533](https://arxiv.org/abs/2012.01533))  
Gratton R. G., Carretta E., Castelli F., 1996, *A&A*, 314, 191  
Harris W. E., 1996, *AJ*, 112, 1487  
Kurucz R. L., 1970, SAO Special Report #309  
Law D. R., Majewski S. R., 2010, *ApJ*, 718, 1128  
Massari D., Koppelman H. H., Helmi A., 2019, *A&A*, 630, L4  
Monaco L., Villanova S., Carraro G., Mucciarelli A., Moni Bidin C., 2018, *A&A*, 616, A181  
Moreno E., Pichardo B., Schuster W. J., 2015, *MNRAS*, 451, 705  
Piotto G. et al., 2015, *AJ*, 149, 91  
Ramírez I., Meléndez J., 2005, *ApJ*, 626, 465  
Renzini A. et al., 2015, *MNRAS*, 454, 4197  
Robin A. C., Reylé C., Derrière S., Picaud S., 2003, *A&A*, 409, 523  
Robin A. C., Reylé C., Fliri J., Czekaj M., Robert C. P., Martins A. M. M., 2014, *A&A*, 569, A13  
Salinas R., Strader J., 2015, *ApJ*, 809, 169  
Sanders J. L., Smith L., Evans N. W., 2019, *MNRAS*, 488, 4552  
Sbordone L., Bonifacio P., Marconi G., Buonanno R., Zaggia S., 2005, *A&A*, 437, 905  
Sirianni M. et al., 2005, *PASP*, 117, 1049  
Snedden C., 1973, *ApJ*, 184, 839  
Stetson P. B., 1987, *PASP*, 99, 191  
Stetson P. B., 1994, *PASP*, 106, 250  
Tautvaišienė G., Wallerstein G., Geisler D., Gonzalez G., Charbonnel C., 2004, *AJ*, 127, 373  
Villanova S., Geisler D., Carraro G., Moni Bidin C., Muñoz C., 2013, *ApJ*, 778, 186 (V13)

This paper has been typeset from a  $\text{\LaTeX}$  file prepared by the author.